Ionics (2019) 25:607–616
https://doi.org/10.1007/s11581-018-2684-2

ORIGINAL PAPER

h-MoO_3/Activated carbon nanocomposites for electrochemical applications

D. N. Sangeetha[1] · D. Krishna Bhat[2] · M. Selvakumar[1]

Received: 27 June 2018 / Revised: 2 August 2018 / Accepted: 6 August 2018 / Published online: 22 August 2018

Abstract

MoO_3 nanorods were synthesized through the microwave method and the nanocomposites of MoO_3/activated carbon were prepared for supercapacitor and hydrogen evolution reaction (HER). The XRD pattern revealed that the prepared MoO_3 has a hexagonal phase (h-MoO_3). The as-prepared h-MoO_3 was composited with activated carbon (AC) and tested for supercapacitor studies. The fabricated supercapacitor exhibited an appreciable specific capacitance, power density, and energy densities. Further, dedoping of nitrogen in the doped AC creates defects on AC (DAC). These DAC/MoO_3 nanocomposites were prepared and tested for its electrocatalytic activity towards hydrogen evolution reactions. DAC/MoO_3 nanocomposite showed much higher electrocatalytic activity than the neat MoO_3.

Keywords h-MoO_3 · Supercapacitors · Specific capacitance · Hydrogen evolution reactions

Introduction

The increasing demand for energy around the globe enforces the utilization of clean and abundantly available renewable resources to meet the future energy demands. To add on to these problems, the rapid use of fossil fuels for various purposes causes the linear decrease in the number of fossil fuels and is responsible for several environmental problems around the globe. Hence, there is a vital requirement of renewable sources, over fossil fuels for energy storage and conversion. Rapid search is on the next generation energy storage and conversion materials. Supercapacitors bridge batteries and capacitors, owing to high power density, faster charge-discharge rate (few seconds), longer shelf-life, and prolonged cycle stability in aqueous as well as non-aqueous electrolytes with high efficiency [1–4]. In simple terms, these could be regarded as the non-polluting power sources. The electrode material for supercapacitors is categorized as (a) high surface area carbon-based materials like activated carbon (AC), carbon aerogels, single and multiwalled carbon nanotubes, templated porous carbon and graphene [5–8], (b) pseudocapacitor materials including conducting polymers and transition-metal oxides—NiO, RuO_2, MnO_2, MoO_3 [9, 10]. A clean energy source, hydrogen, has acquired a great interest in recent years due to its eco-friendly nature, non-carbonaceous matter emission when burnt, and high energy density characteristics. Although H_2 has certain merits, the production of H_2 consumes a significant amount of energy, which in turn hinders its commercialization. Thus, there is a constant search for highly electroactive materials for hydrogen evolution reaction (HER) [11, 12].

Biomass-derived AC is of great interest due to its exclusive characteristics such as large specific surface area (~ 4000 $m^2\ g^{-1}$), low cost, higher endurance, good electric conductivity, less corrosiveness, and also wide operating temperature. High surface area AC was synthesized using several biomass precursors like apricot seeds, potato starch, seaweed, corncob, gelatin, egg-white, and prawn-shells [13–19]. The carbon materials are not generally considered to be active towards various electrochemical reactions due to their sluggish nature. But these materials can be converted into electrochemically active material by creating defects in their lattice. These defects can be created through doping or dedoping the heteroatoms [20, 21]. Various research groups around the globe are working head on, so as to increase the specific energy and power of the supercapacitors. The attempts include metal

✉ M. Selvakumar
chemselva78@gmail.com

[1] Department of Chemistry, Manipal Institute of Technology, Manipal Academy of Higher Education, Manipal, Karnataka 576104, India

[2] Department of Chemistry, National Institute of Technology, Surathkal, Mangalore 575025, India

oxide nanostructures derived from metal-organic frameworks with tunable structure and their composition [22, 23]; growth of conducting polymer array on the porous carbon [24]; electroless plating producing surface deposition of nanoparticles on AC [25]; multilayer approach [26]; composites of EDLCs materials with the pseudocapacitive materials [27, 28]. Lee JH et al. demonstrated the use of the composite in fabricating cylindrical hybrid supercapacitor. High surface activated carbon was used as the positive electrode and Nb-doped $H_2Ti_{12}O_{25}$(HTO) giving $H_2Ti_{12-x}Nb_xO_{25}$, as the negative electrode. The concentration of the dopant was varied from $0 \le x \le 0.6$ to study the performance of the supercapacitor. Among the various ratios, $H_2Ti_{11.85}Nb_{0.15}O_{25}$ retained 84% of the initial capacitance even after 10,000 cycles [29]. The same group improvised the negative electrode material by using carbon/$AlPO_4$-coated HTO, in the fabrication of hybrid supercapacitors. This combination yielded a very high energy and power density reaching up to 46.3 W h kg^{-1} and 12,223.9 W kg^{-1}, respectively [30]. Lee B-G et al. used the combination of AC with granular $Li4Ti5O_{12}$ (LTO) to study the improved performance of the asymmetric hybrid supercapacitors at different current densities [31]. Transition-metal oxides like MoO_3 are of great interest for supercapacitor and HER, due to their excellent reduction-oxidation (redox) properties ($M^{n+} + e^- \rightarrow M^{n\pm1}$). The process of charge storage mechanism is due to the highly reversible surface redox reactions termed as pseudocapacitance. The unique structure of them helps in faster electron transport for HER. The three crystalline polymorphs of MoO_3 include α-MoO_3 (orthorhombic), β-MoO_3 (monoclinic), and h-MoO_3 (hexagonal) [32]. MoO_3 has been synthesized in different morphology such as nanorods, nanosheets, nanodots, and nanobelts, tested for two applications, supercapacitors and HER [33–37]. The poor inherent conductivity of MoO_3 avoids the use of it in a single component MoO_3 electrode system. Thus, by preparing composites of MoO_3 with the AC, enhanced specific capacitance (SC) and improved catalytic activity of MoO_3 is observed [38, 39].

Although metastable h-MoO_3 shows enhanced electrochemical properties, its synthesis is difficult compared to other stable forms. In view of this, in this paper, we have demonstrated, quick and simple microwave-assisted synthesis of h-MoO_3 using a CTAB surfactant to control the size parameters. The sustainable synthesis of AC using the Tendu leaves has been reported in the previous work. AC/MoO_3 composites were tested for supercapacitor applications through cyclic voltammetry, galvanostatic charge-discharge, and AC-impedance studies. Further, we processed the AC obtained from the Tendu leaves to create defective sites (DAC) and studied the electrocatalytic activity of DAC/MoO_3 composites towards hydrogen evolution reaction through linear sweep voltammetry and Tafel plots.

Materials and methods

The synthesis of AC and DAC was done following the literature procedure [40–42]. Synthesis of MoO_3 was carried out by dissolving a mixture of 0.49 g of ammonium molybdate tetrahydrate ($(NH_4)_6Mo_7O_{24}{\cdot}4H_2O$) and 0.36 g of CTAB in 20-mL distilled water with continuous stirring for 30 min. To this solution, 3M HNO_3 (7.50 mL) was added and was placed in a microwave oven maintained at 150 °C for 30 mins. The precipitate obtained was then collected and dried [43]. X-ray diffraction (XRD) patterns were obtained between $2\theta = 10$ and 70° with the help of Bruker Miniflex 600 model. Scanning electron microscopy (SEM) was used to analyze the surface morphology of the samples using ZEISS EVO18 special edition. Transmission electron microscopy (TEM) was obtained using Philips CM 200. X-ray photoelectron spectroscopy (XPS) was determined using a nonmonochromatic Al Kα source (1486.6 eV) with a pass energy of 50.0 eV.

Electrochemical characterization and fabrication of supercapacitor electrodes

All the electrochemical measurements were carried out using BioLogic SP-150. Electrochemical impedance spectroscopy (EIS) was performed in the frequency range of 10 mHz to 1 MHz and AC amplitude of 10 mV with respect to the open circuit potential. EIS measurements initially were performed in a three-electrode system—counter (Pt), reference (saturated calomel), and working electrodes (fabricated composite electrode). Cyclic voltammetry (CV) and galvanostatic charge-discharge (GCD) were performed in a two-electrode working setup.

Different weight ratio—1:1, 1:2, 1:3, 2:1, and 3:1, of AC and the MoO_3, were mixed to form composites as given below. The ratio with lesser impedance was chosen for studying the further electrochemical properties. The procedure to fabricate the working electrode was as follows. AC/MoO_3, acetylene black, and binder mixture (poly (vinylidene fluoride) in N-methylpyrrolidone) were taken in 80:15:5 weight ratio and finely mixed to give a homogeneous slurry. This mixture was then coated on a stainless steel (SS) current collector of surface area 1 cm^2 and let to dry. This is taken to be the working electrode. The weight of the working electrode was maintained to be ≈ 5 mg cm^{-2}. The assembly of two AC/MoO_3 electrodes separated by polypropylene separator will be termed as symmetric supercapacitor electrode throughout whereas the assembly of AC electrode as positive and AC/MoO_3 electrode as negative electrodes separated by the separator will be regarded as a hybrid supercapacitor. 1M Na_2SO_4 was chosen as the electrolyte for supercapacitor studies.

Preparation of the electrode for electrochemical HER work was done as follows. Initially, the AC was doped with nitrogen

through a hydrothermal method using urea as a dopant. This was termed as nitrogen-doped AC (NAC). This NAC was later annealed in the N_2 atmosphere at 800 °C for 2 h to create defects in the AC. This was labeled as DAC [40]. 1:1 weight ratio of NAC/MoO_3, DAC/MoO_3 composites was sonicated with 50-μL Nafion and 250-μL water for 30 min to ensure proper dispersion. This mixture was drop cast on the glassy carbon electrode. N_2 saturated 0.5-M H_2SO_4 electrolyte was chosen for HER in three-electrode systems using Ag/AgCl as a reference and Pt as a counter electrode.

Results and discussion

Figure 1a shows densely dispersed MoO_3 nanorods. These nanorods showed an irregularity in their size and shape. Figure 1b represents the XRD of MoO_3 and the pattern indicates the metastable hexagonal phase of MoO_3 (h-MoO_3). The compound has single crystalline hexagonal phase. No secondary impurity peaks that correspond to other polymorphs of MoO_3 were observed. The strong diffraction peaks at $2\theta =$ 10.35°, 20.04°, 26.3°, and 29.9° are indexed to the (100), (200), (210), and (300) crystal phases of h-MoO_3 with reference to JCPDS-21-0569. To calculate the average crystallite size (τ) of the synthesized MoO_3, Scherrer's formula is used.

$$\tau = \frac{K\lambda}{\beta\cos\theta}$$

K is the shape factor whose value is taken to be 0.9, λ is the x-ray wavelength, β is the line broadening at half the maximum intensity also known as the full width half maximum (FWHM), and θ is the Bragg angle. The average crystallite size was found to be ≈ 142 nm. The high-intensity peak was observed at 25.80° and is noticed to be sharp with slight broadening. This broadening of the highest intensity peak is due to the reduced crystallite size. When the particle size is reduced to the nanoscale, the ratio of the disordered atoms at the surface of particles with the ordered atoms in the center of the nanoparticles is found to be higher than that in the bulk MoO_3. This is reflected as the broadening of the XRD peaks. In the h-MoO_3 phase, the tunnel along the c-direction probably contains water molecules or cations. These molecules or cations are bounded by 12 MoO_6 octahedra. These are linked in the zigzag chain fashion by sharing the corners and the corners align along the a, b directions [44]. The formation of metastable h-MoO_3 was affected by the solvent used, the concentration of HNO_3, and reaction time. The better crystallinity was observed when water was used as the solvent medium. The crystallite size was calculated to be 150 nm. Figure 1c corresponds to TEM images of MoO_3. Particles of 1D-rod shaped, stacked together to form a dense structure were observed. SAED was carried out to identify the crystal phase of the h-MoO_3. The hexagonal dot pattern was obtained, and the corresponding phases have also been identified in the SAED patterns [45–47]. The measured lattice spacing corresponds to (220), (210), (200), and (100) plane of h-MoO3 that was found in a match with the obtained XRD data.

Supercapacitor studies of symmetric and hybrid electrodes

The frequency range of 10^3–10^5 Hz and potential of 10 mV with respect to open circuit potential were chosen to carry out the EIS measurements. In 5–10 mV, the system was linear, and for other potentials, the system was nonlinear. When the potential was increased from lower value to higher value, the tail of the impedance curve (Warburg) approached 90°. Pseudocapacitance nature dominated at a lower frequency with respect to the potential of the material. The R_{Ct} value also decreased, when the applied potential was increased, due to the reduced length of diffusion [48]. All the ratios of AC/MoO_3 exhibited similar patterned impedance plots as shown in Fig. 2a. MoO_3 showed a very high resistance value of 4200 Ω whereas AC alone showed the much lesser resistance of 125 Ω. The prepared composites with different ratios of AC/MoO_3 namely, 1:1, 1:2, 1:3, 2:1, and 3:1 showed a resistance of 36, 365, 1356, 76, and 43 Ω, respectively.

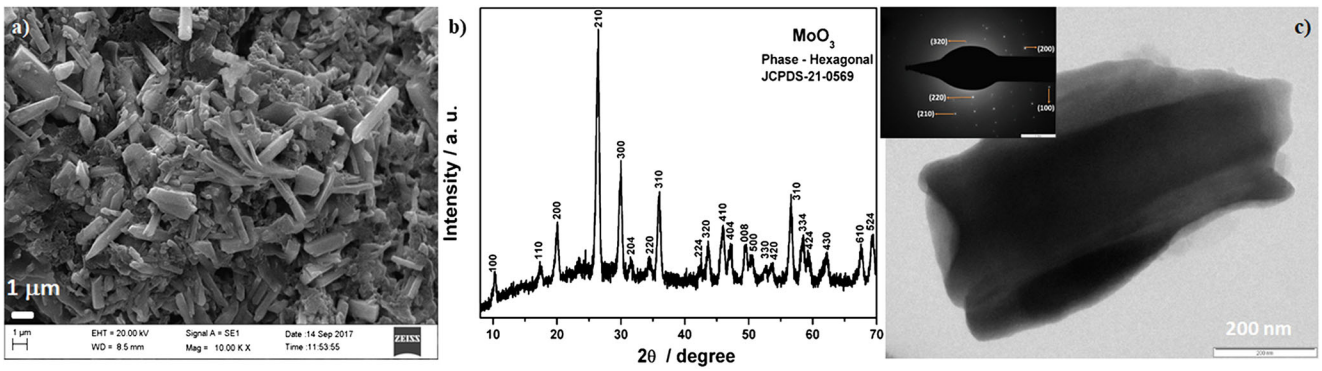

Fig. 1 MoO_3. **a** SEM image; **b** XRD results; **c** TEM image. Inset: electron diffraction pattern

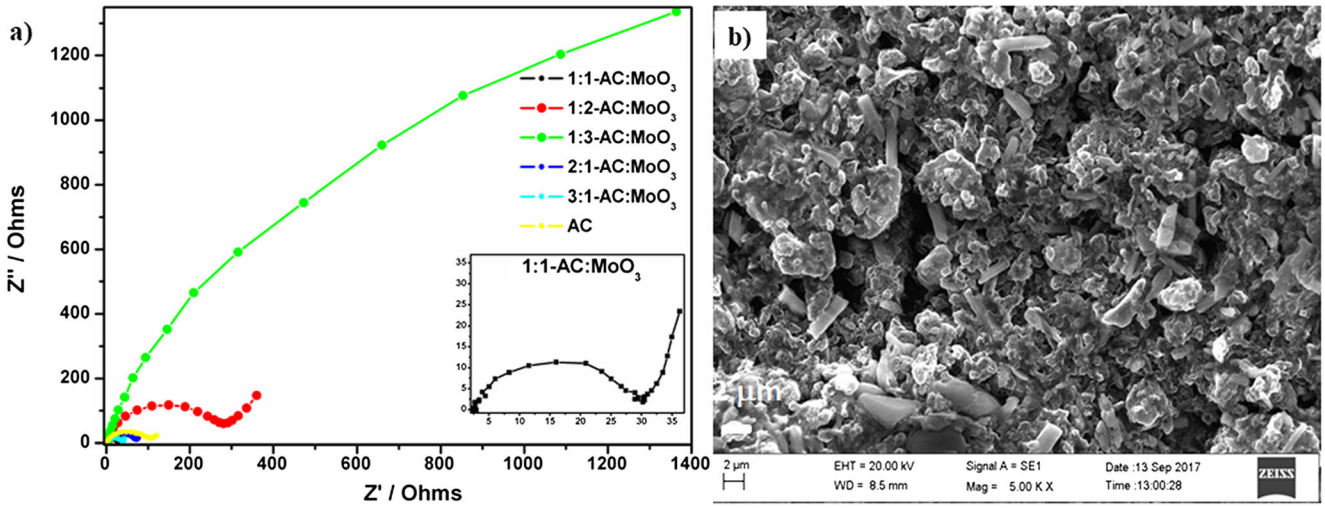

Fig. 2 AC/MoO_3 composites. **a** Nyquist plots of different ratios namely, 1:1, 1:2, 1:3, 2:1, and 3:1 of AC/MoO_3; **b** SEM images of 1:1 AC/MoS_2

Among the above, 1:1 AC/MoO_3 nanocomposite showed better performance with the lesser resistance of 36 Ω. Thus, the ratio 1:1 AC/MoO_3 was adjudged as the best composite and used for the fabrication of symmetric and hybrid supercapacitors.

To test the performance of both symmetric and hybrid supercapacitor electrodes, CV and GCD measurements were carried out. The CV and GCD profiles measured at a range of scan rates and current densities are shown in Figs. 3 a and 4a and Figs. 3 b and 4b, respectively. Figure 2b represents the SEM image of the 1:1 AC/MoO_3. The composites of AC/MoO_3 exhibit the morphological features of both AC and MoO_3. Since the potential of MoO_3 was measured towards the negative potential range (− 0.8 to 0.0 V) and that of AC towards the positive potential range (0 to 1.0 V), the operating cell voltage extended from − 0.8 to 1.0 V for both the supercapacitors. A quasi-rectangular shape was observed, in this potential range, when the CV study was carried out (Figs. 3a and 4a). The double layer behavior of AC along with the pseudocapacitive behavior of MoO_3 is accountable for such a response. Due to the pseudocapacitive nature of MoO_3, there is a slight modification in the quasi-rectangular behavior as seen in Figs. 3 a and 4a. It is noticeable that as the scan rates vary, the rectangular profile is retained, and this infers good

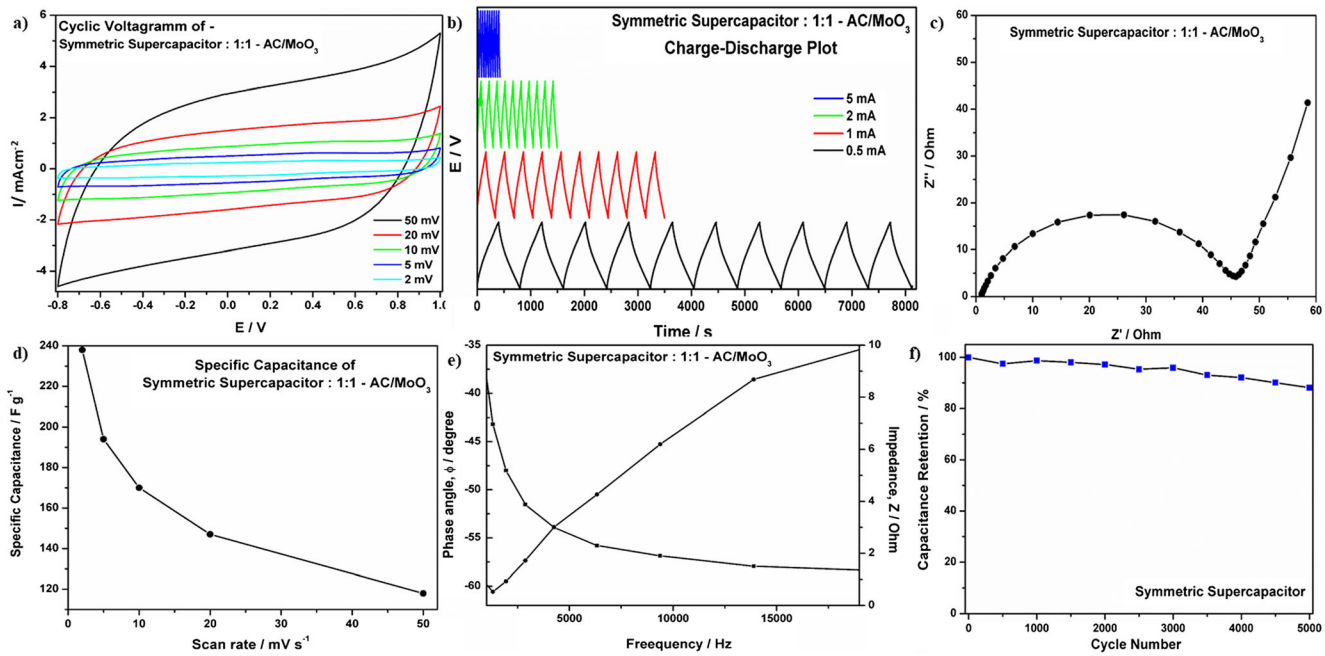

Fig. 3 Electrochemical properties of Symmetric Supercapacitors in 1-M Na_2SO_4. **a** CV curves recorded at different scan rates, **b** galvanostatic charge-discharge profile with different current densities, **c** Nyquist plot, **d** specific capacitance at different scan rates, **e** time constant plot, and **f** capacitance retention over 5000 cycles

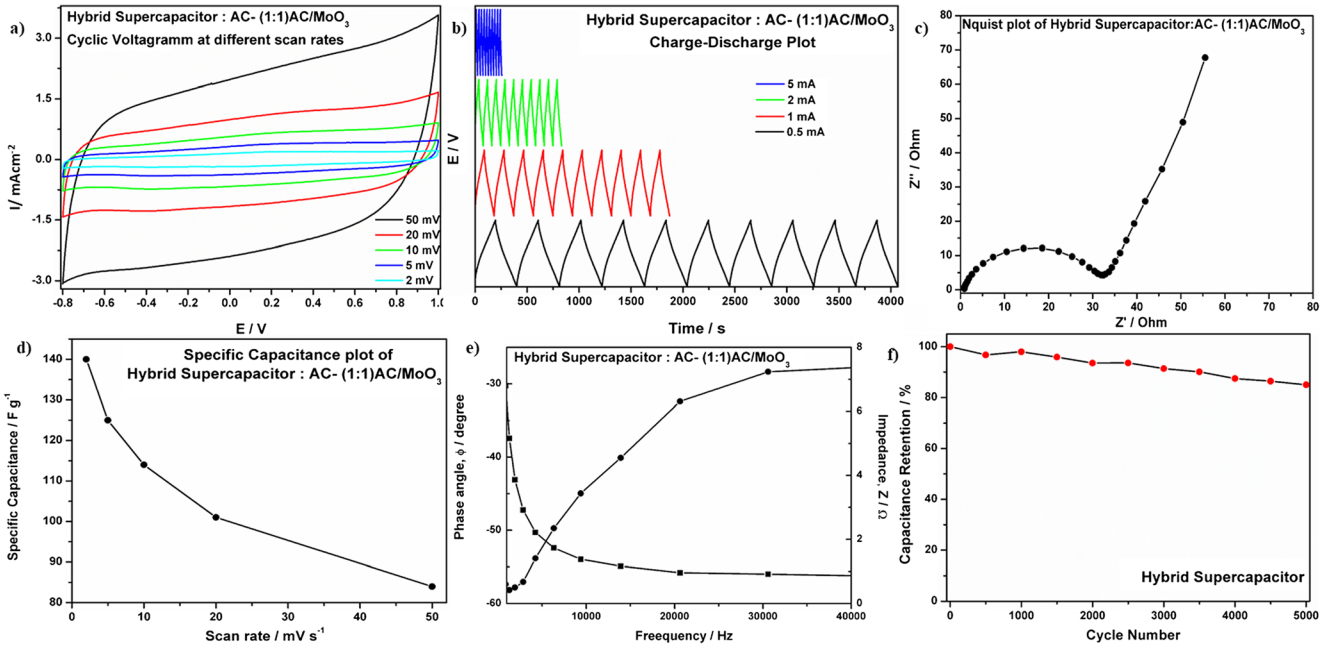

Fig. 4 Electrochemical properties of hybrid supercapacitors in 1-M Na_2SO_4. **a** CV curves recorded at different scan rates, **b** galvanostatic charge-discharge profile with different current densities, **c** Nyquist plot, **d** specific capacitance at different scan rates, **e** time constant plot, and **f** capacitance retention over 5000 cycles

specific capacitance and faster charge transferability of the composite material. Nyquist plots for both the supercapacitors are shown in Figs. 3c and 4c. A linear line at a lower frequency region represents lower charge transfer resistance and a pronounced capacitive nature with slight diffusion resistance, respectively. However, in the Nyquist plot for both symmetric and hybrid supercapacitors as shown in Figs. 3 c and 4c, the arc in the high-frequency region is the contribution of the fast electron diffusion which further gives charge transfer resistance of the electrode material. In the high-frequency region, the reduced width of the arc is due to the shortened path for electron transport within the composite electrode material. The slope of the curve is termed as Warburg resistance and is observed due to the frequency dependence of ion diffusion/transport in the Na_2SO_4 to the electrode surface. The charge transfer resistance was calculated to be 45 Ω and the Warburg diffusion element (Z_w) was found to be equal to 59 Ω for symmetric supercapacitors. The SC (C_S in F g^{-1}) value from CV plot at various scan rates was calculated using the formula

$$C_S = \frac{2A}{\Delta V \times v \times m} \quad (1)$$

here A represents an integral area of CV loop, ΔV the potential window, v the scan rate, and m represents the mass of the material at each electrode [49]. As shown in Figs. 3 e and 4e, the SC decreases as the scan rate increases and a maximum value was obtained for 2 mVs^{-1}. When the current density is low, the electrolyte ions get sufficient time for complete movement throughout the surface of the electrode material. Hence, the higher capacitance value is observed at lower current densities. Whereas, when the current density is higher, there occurs incomplete diffusion of electrolyte ions and hence the capacitance value decreases. The SC values of symmetric and hybrid supercapacitors were observed to be 238 and 140 F g^{-1} at 2 mVs^{-1}, respectively. The supercapacitor performances of the AC/MoO_3 compared with those of the reported literature is summarized in Table 1. GCD plots of symmetric and hybrid supercapacitors at different current densities are shown in the Figs. 3 b and 4b, respectively. During charging, there is an increase in the accumulation of charges, i.e., Na^+ ions at the positive and SO_4^- at the negative electrode. There is an enhance in the potential difference. Once the capacitor is fully charged, the current passing through the circuit starts from a maximum value and then falls to 0. During the discharging process, as the current flows through the circuit the potential difference between the plates decreases. The plates individually attain electrical neutrality. The schematic representation of charge/discharge is shown below.

A very minute IR drop was observed in the GCD plots as shown in Figs. 3 b and 4b. And also, the shape of the profile is symmetric and a nonlinear triangular. The nonlinearity of the discharge curve is evident for good capacitive behavior. Also, the profile accounts for the nearly ideal charging/discharging performance with good reversibility of the electrode material. It is due to the weak van der Wall forces that stack the several sheets together to form irregular morphology. The space between these sheets helps in the electrolyte ion intercalation and deintercalation during charging and discharging of MoO_3

Table 1 Comparison of supercapacitor performance of the present work with the literature

Material	Specific capacitance	Energy density (W h kg^{-1})	Power density (W kg^{-1})	References
α-MoO_3 nanorods	30 F g^{-1} in 1-M H_2SO_4	17	425	[25]
AC/$H_2Ti_{11.85}Nb_{0.15}O_{25}$	78.4 F g^{-1} in 1.5-M $LiBF_4$	24.3	1794.6	[29]
Carbon/AlPO4 hybrid-coated $H_2Ti_{12}O_{25}$/AC	58.19 F g^{-1} in 1.5-M $LiPF_6$ solution in 1:1 ethylene carbonate: dimethyl carbonate	46.3	12,223.9	[30]
Granule $Li_4Ti_5O_{12}$/AC	46.4 F g^{-1} in 1.5-M $LiPF_6$ solution in 1:1 ethylene carbonate: dimethyl carbonate	___	___	[31]
MoO_3/C matrix	179 F g^{-1} in 1-M H_2SO_4	___	___	[35]
MoO_3 nanodots/MWCNTs	103 F g^{-1} in 1-M $LiClO_4$ in propylene carbonate	36.57	1870	[37]
PANI nanotubes/MoO_3 nanobelts	518 F g^{-1} in 1-M H_2SO_4	71.9	254	[50]
Branchlike MoO_3/polypyrrole	129 F g^{-1} in 1-M Na_2SO_4	___	___	[51]
MoO_3/C	331 F g^{-1} in 1-M H_2SO_4	41.2	12,000	[52]
Graphene/MoO_3 nanospheres// graphene/MoO_3 nanosheets	307 F g^{-1} in 1-M Na_2SO_4	42.6	276	[53]
h-MoO_3 microrods	194 F g^{-1} in 1-M Na_2SO_4	7.33	1200	[54]
α-MoO_3 nanobelts	369 F g^{-1} in 0.5-M Li_2SO_4			
α-MoO_3 nanoplates	280 F g^{-1} in 0.5-M Li_2SO_4			
α-MoO_3 nanowires	110 F g^{-1} in 0.5-M Li_2SO_4			
α-MoO_3 nanorods	30 F g^{-1} in 0.5-M Li_2SO_4			[55]
MoO_3 nanosheets	540 F g^{-1} in 1-M $LiClO_4$ in propylene carbonate	___	___	[35]
AC/MoO_3	225 F g^{-1} in 1-M Na_2SO_4	27	225	Present Work

electrodes. Additionally, the 1-D morphology of MoO_3 also contributes to the faster electron transport, resulting in the enhanced SC.

The SC ($C_{S'}$ in F g^{-1}) from the charge-discharge plot was calculated using the below formula,

$$CS' = \frac{I\Delta t}{\Delta V m} \tag{2}$$

I represents the current density and Δt is the discharge time. 2 mA/cm^2 owes to a maximum SC and the capacitance value reduced as the current density increased. The SC calculated from charge-discharge profile was found to be 156 and 128 F g^{-1} for symmetric and hybrid supercapacitors, respectively. The charge transfer resistance calculated was 31 Ω and the Warburg diffusion element (Z_w) observed for hybrid supercapacitors was 56 Ω. From the results obtained, it is evident that the symmetric supercapacitors gave a higher SC than that of the hybrid supercapacitors.

Figures 3 e and 4e show normalized imaginary part or the reactive power |Q|/|S| (impedance) and active part or the active power |P|/|S| (phase angle) of the complex power versus frequency plot. The time constants for the symmetric and hybrid supercapacitor were calculated from these plots. As the frequency was decreased, |Q|/|S| increased, reaching a maximum power. In the lower frequency region, the supercapacitor behaved like a pure capacitor. The normalized active power corresponds to the power dissipated into the system. At a lower frequency region, i.e., when the supercapacitor behaved as the pure capacitor, the maximum of the |Q|/|S| was reached. The two plots cross over when |P| = |Q|, i.e., when φ = 45° that in turn corresponds to the time constant τ_0. The time constant calculated was 1.6 ms. This indicates that the present system highly efficient at lower frequencies [56, 57].

The energy density (E in W h kg^{-1}) and the power density (P in W kg^{-1}) were calculated from the following equations:

$$E = \frac{1}{2} C_S (\Delta V)^2 \tag{3}$$

$$P = \frac{E}{\Delta t} \tag{4}$$

$$ESR = \frac{iR_{\text{drop}}}{2 \times I} \tag{5}$$

where C_S is the SC, ΔV represents the potential window, Δt is the discharge time after iR_{drop}. Five thousand cycles from charge-discharge at a current density of 10 mA was performed to check the stability of the electrode material. Of the initial capacitance, ~87 and 85% were retained for symmetric and hybrid supercapacitors respectively even after 5000 cycles. The SC calculated from cyclic voltammetry and charge/discharge, the energy density, power density, and ESR values calculated from charge/discharge plot for both AC/MoO_3 symmetric and hybrid supercapacitor performance is summarized in Table 2.

Table 2 Summary of the calculated values of specific capacitance, ESR, charge transfer resistance, energy density and power density of symmetric, and hybrid supercapacitors

Type	Specific capacitance from CV (F g^{-1})	Specific capacitance from GCD (F g^{-1})	ESR (Ω)	Charge transfer resistance (Ω)	Energy density (W h $kg^{-1)}$	Power density (W kg^{-1})
Symmetric supercapacitor	238	156	0.974	45	27	225
Hybrid supercapacitor	140	128	0.885	31	13	200

Hydrogen evolution reaction (HER)

The total hydrogen evolution reaction, in acidic medium (H_2SO_4) on DAC/MoO_3 surface (A), can be written as follows,

Step I: Volmer reaction—wherein electrochemical adsorption of hydrogen takes place on the DAC/MoO_3 composite surface. The surface provides an electron giving an intermediate adsorbed state on the surface.

$$H_3O^+ + e^- + A \rightarrow AH^*_{adsorption} + H_2O \quad (6)$$

Step II: Tafel reaction—a combination

$$2\,AH^*_{adsorption} \rightarrow 2A + H_2\uparrow \quad (7)$$

Step III: Heyrovsky reaction—desorption of H_2

$$AH^*_{adsorption} + H_3O^+ + e^- \rightarrow H_2\uparrow + H_2O \quad (8)$$

where the * denotes a site on the surface and H* denotes a hydrogen atom adsorbed on the surface. Based on the calculated value of overpotential, HER follows either Tafel (step II) or Heyrovsky (step III) [58]. Figure 6b shows the LSV for HER for different composites. The calculated current density was 76 mA cm^{-2}. The potential range of 0.0 to − 0.4 V was chosen to carry out HER. The DAC used in the composite material owes to the nonlinearity of the Tafel slope. The onset potential was found to be − 0.19 V for DAC/MoO_3. The Tafel slope value calculated from LSV was − 92 mV dec^{-1} for DAC/MoO_3 and − 110 mV dec^{-1} for NAC/MoO_3 nanocomposites and that for MoO_3 was found to be − 176 mV dec^{-1}. The experimental overpotential value for DAC/MoO_3 was found to be, − 50.2 mV dec^{-1} at a current density of 10 mA cm^{-2}. The rate-determining step for HER can be identified using the Tafel slope values, that correspond to above mentioned steps (7 and 8)—Tafel, Heyrovsky reactions. In step I, the Volmer reaction is taken to be the rate-controlling step of HER. In a particular set of conditions, a slope of 120 mV dec^{-1} is obtained in this step. If the reaction proceeds through steps II and III, the Tafel slope values of 30 or 40 mV dec^{-1} will be detected. Complete H_2 molecule evolution does not proceed through a single step but instead

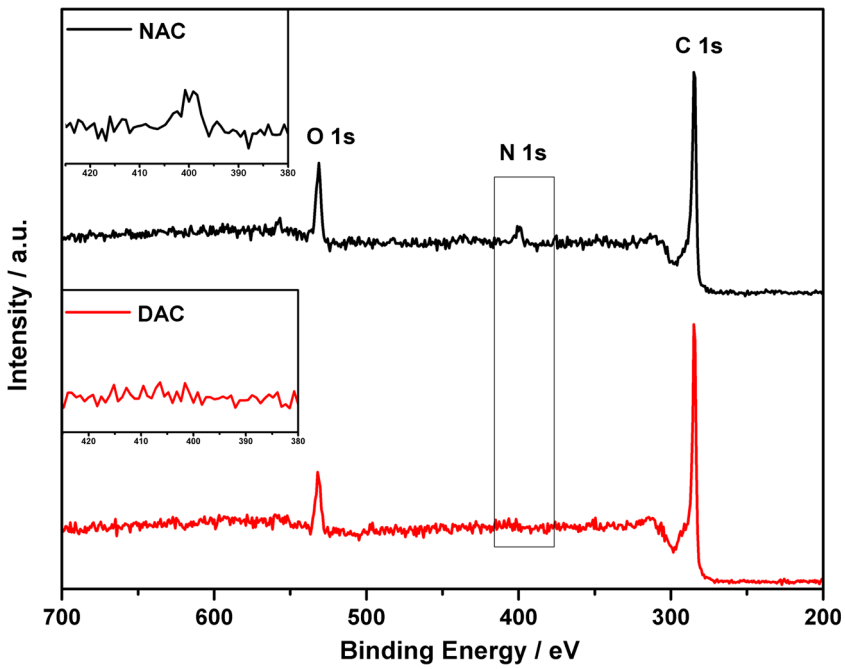

Fig. 5 XPS spectra of NAC and DAC

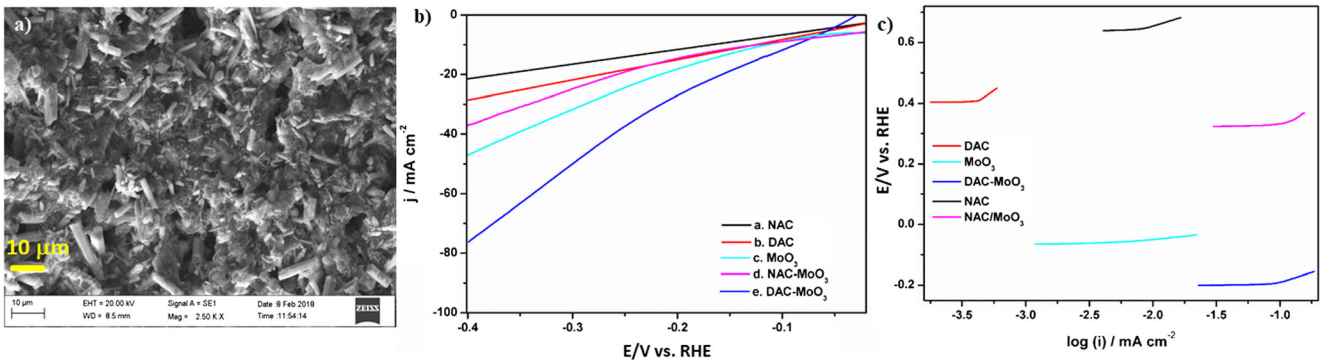

Fig. 6 **a** SEM images of DAC/MoO_3, **b** polarization curves evaluating the HER performance of DAC/MoO_3, and **c** current density vs overvoltage plot

proceeds through Volmer-Heyrovsky mechanism or Volmer–Tafel mechanism. In the present study, the results obtained shows that the HER from DAC/MoO_3 nanocomposites follows Volmer-Heyrovsky mechanism. The lesser value of the Tafel slope for DAC/MoO_3 nanocomposite material displays better hydrogen evolution at the electrode surface. The defective sites mainly contribute to this enhancement [20]. When the activated carbon (AC) is doped with nitrogen and further when this doped nitrogen is dedoped through high-temperature annealing (800 °C) under the N_2 atmosphere, there are defective sites observed due to the removal of nitrogen atoms [40]. From the XPS plots shown in Fig. 5, two common peaks for both NAC and DAC are noticeable. The first common peak appears at ≈ 285 eV that corresponds to the 1s C. While the next peak appears at ≈ 530 eV and corresponds to 1s O. However, the peak at ≈ 400 is observed only in NAC which corresponds to 1s N. This is due to the doped N in NAC which disappears in the case of DAC wherein the N is been removed to create defective sites [41, 59]. In addition to the defects on AC, the distribution of MoO_3 over AC greatly influence the reduction of Tafel slope value. The 1-D morphology of MoO_3 is an additional advantage to enhance the electrochemical activity. These facilitate the electron transport along the nanorod axis, i.e., electrons are thus confined in one direction. This can also act as a driving force for faster electron movement and thus enhances electroactivity. The interconnected network of uniformly distributed MoO_3 on the DAC (Fig. 6a) thus facilitates the fast electron transport in the DAC.

Table 3 Electrocatalytic performance of the electrocatalyst towards HER

Electrocatalyst	Onset potential (*V* vs Ag/AgCl)	Tafel slope (mV/dec)	Overpotential (mV/dec)
DAC/MoO_3	− 0.19	− 92	− 50.2

The reduction in the Tafel slope value of DAC, compared with that of DAC/MoO_3 shows that MoO_3 contributes towards HER in DAC/MoO_3 nanocomposites. While in the case of HER, 100 cyclic voltammetry cycles were run at a scan rate of 10 mV s^{-1} to check the stability of the electrode material. The material was stable upto 100 cycles in the acidic medium and maintains good HER. Table 3 summarizes the electrocatalytic properties of DAC/MoO_3, towards HER. The results suggested that the composite is a potential material for hydrogen evolution in the acidic medium. Activated carbon is a sluggish material towards electrochemical hydrogen evolution and does not show significant HER activity even when composited with electrochemically active MoO_3. But when defects are formed in activated carbon, the material exhibits enhanced HER, which very clearly indicates the active role of defects in the process.

Conclusion

In summary, here we report the synthesis of hexagonal phase MoO_3 via a simple and faster microwave synthesis route. The composite materials of AC/MoO_3 show the excellent performance as symmetric and hybrid supercapacitors. The fabricated symmetric supercapacitor exhibited a higher SC of 238 F g^{-1}, power density of 225 W kg^{-1} at a current density of 1 mA than compared to hybrid supercapacitor SC of 140 F g^{-1}, power density 200 W kg^{-1}. The material also has a large potential window of 1.8 V. The prepared DAC/MoO_3 composite showed a Tafel slope of 92 mV dec^{-1} for hydrogen evolution reaction. Hence, AC/MoO_3 and DAC/MoO_3 composites can be considered as a potential next-generation materials for supercapacitor and hydrogen evolution reaction.

Acknowledgments The author acknowledges Manipal Academy of Higher Education for the research fellowship, the laboratory, and instrumentation facilities. Also, the authors are thankful to the Sophisticated Analytical Instrument Facility, IIT-Bombay, and Indian Institute of Technology, Kharagpur for the characterization facility.

References

1. Winter M, Brodd RJ (2005) What are batteries, fuel cells, and supercapacitors? Chem Rev 105:4245–4269
2. Eftekhari A, Fang B (2017) Electrochemical hydrogen storage: opportunities for fuel storage, batteries, fuel cells, and supercapacitors. Int J Hydrog Energy 42:25143–25165
3. Davies A, Yu A (2011) Material advancements in supercapacitors: from activated carbon to carbon nanotube and graphene. Can J Chem Eng 89:1342–1357
4. Gu W, Yushin G (2014) Review of nanostructured carbon materials for electrochemical capacitor applications: advantages and limitations of activated carbon, carbide-derived carbon, zeolite-templated carbon, carbon aerogels, carbon nanotubes, onion-like carbon, and graphene. WIREs Energy Environ 3:424–473
5. Zhang Q, Uchaker E, Candelaria SL, Cao G (2013) Nanomaterials for energy conversion and storage. Chem Soc Rev 42:3127–3171
6. Yan J, Wang Q, Wei T, Fan Z (2014) Recent advances in design and fabrication of electrochemical supercapacitors with high energy densities. Adv Energy Mater 4:1300816
7. Tang J, Yamauchi Y (2016) MOF morphologies in control. Nat Chem 8:638–639
8. Salunkhe RR, Lee Y-H, Chang K-H, Li J-M, Simon P, Tang J, Torad NL, Hu C-C, Yamauchi Y (2014) Nanoarchitectured graphene-based supercapacitors for next-generation energy-storage applications. Chem Eur J 20:13838–13852
9. Wang G, Zhang L, Zhang J (2012) A review of electrode materials for electrochemical supercapacitors. Chem Soc Rev 41:797–828
10. Pang H, Zhang GX, Xiao X, Li B, Gu P, Xue HG (2017) Transition metal oxides with one-dimensional/one-dimensional-analog nanostructures for advanced supercapacitors. J Mater Chem A 5:8155–8186
11. Zou X, Zhang Y (2015) Noble metal-free hydrogen evolution catalysts for water splitting. Chem Soc Rev 44:5148–5180
12. Faber MS, Jin S (2014) Earth-abundant inorganic electrocatalysts and their nanostructures for energy conversion applications. Energy Environ Sci 7:3519–3542
13. Ostafiychuk BK, Budzulyak IM, Rachiy BI, Vashchynsky VM, Mandzyuk VI, Lisovsky RP, Shyyko LO (2015) Thermochemically activated carbon as an electrode material for supercapacitors. Nanoscale Res Lett 10:65
14. Wei L, Sevilla M, Fuertes AB, Mokaya R, Yushin G (2011) Hydrothermal carbonization of abundant renewable natural organic chemicals for high-performance supercapacitor electrodes. Adv Energy Mater 1:356–361
15. Pinero ER, Cadek M, Beguin F (2009) Tuning carbon materials for supercapacitors by direct pyrolysis of seaweeds. Adv Funct Mater 19:1032–1039
16. Karnan M, Subramania K, Srividhya PK, Sathish M (2017) Electrochemical studies on corncob derived activated porous carbon for supercapacitors application in aqueous and non-aqueous electrolytes. Electrochim Acta 228:586–596
17. Xu B, Hou S, Cao G, Wu F, Yang Y (2012) Sustainable nitrogen-doped porous carbon with high surface areas prepared from gelatin for supercapacitors. J Mater Chem 22:19088–19093
18. Li Z, Xu Z, Wang H, Ding J, Zahiri B, Holt CMB, Tanab X, Mitlin D (2014) Colossal pseudocapacitance in a high functionality–high surface area carbon anode doubles the energy of an asymmetric supercapacitor. Energy Environ 7:1708–1718
19. Gaoa F, Qua J, Zhaob Z, Wangb Z, Qiu J (2016) Nitrogen-doped activated carbon derived from prawn shells for high-performance supercapacitors. Electrochim Acta 190:1134–1141
20. Zhao H, Sun C, Jin Z, Wang D-W, Yan X, Chen Z, Zhua G, Yao X (2015) Carbon for the oxygen reduction reaction: a defect mechanism. J Mater Chem A 3:11736–11739
21. Zhao X, Zou X, Yan X, Brown CL, Chen ZG, Zhu G, Yao X (2016) Defect-driven oxygen reduction reaction (ORR) of carbon without any element doping. Inorg Chem Front 3:417–421
22. Salunkhe RR, Kaneti YV, Yamauchi Y (2017) Metal-organic framework-derived nanoporous metal oxides toward supercapacitor applications: progress and prospects. ACS Nano 11:5293–5308
23. Salunkhe RR, Young C, Tang J, Takei T, Ide Y, Kobayashi N, Yamauchi Y (2016) A high-performance supercapacitor cell based on ZIF-9-derived nanoporous carbon using an organic electrolyte. Chem Commun 52:4764–4767
24. Salunkhe RR, Tang J, Kobayashi N, Kim J, Ide Y, Tominaka S, Kim JH, Yamauchi Y (2016) Ultrahigh performance supercapacitors utilizing core-shell, nanoarchitectures, from a metal-organic framework-derived nanoporous carbon and a conducting polyer. Chem Sci 7:5704–5713
25. Teng Y, Liu K, Liu R, Yang Z, Wang L, Jiang H, Ding R, Liu E (2017) A novel copper nanoparticles/bean dregs-based activated carbon composite as pseudocapacitors. Mater Res Bull 89:33–41
26. Sowmya SM (2018) Multi-layered electrode materials based on polyaniline/activated carbon composites for supercapacitor applications. Int J Hydrog Energy 43:4067–4080
27. Umeshbabu E, Rajeshkhanna G, Rao GR (2015) Effect of solvents on the morphology of $NiCo_2O_4$/graphene nanostructures for electrochemical pseudocapacitor application. J Solid State Electrochem 20:1837–1844
28. Lee S-H, Kim JH, Yoon J-R (2018) Laser scribbled graphene cathode for the next generation of high-performance hybrid supercapacitors. Sci Rep 8:8179
29. Lee JH, Kim H-K, Baek E, Pecht M, Lee S-H, Lee Y-H (2016) Improved performance of cylindrical hybrid supercapacitor using activated carbon/niobium doped hydrogen titanate. J Power Sources 301:348–354
30. Lee J-H, Lee S-H (2016) Applications of novel carbon/$AlPO_4$ hybrid-coated $H_2Ti_{12}O_{25}$ as a high-performance anode for cylindrical hybrid supercapacitors. Appl Mater Interfaces 8:28974–28981
31. Lee B-G, Lee S-H (2017) Application of hybrid supercapacitor using granule $Li_4Ti_5O_{12}$/activated carbon with a variation of current density. J Power Sources 342:545–549
32. Nagabhushana GP, Samrat D, Chandrappa GT (2014) α-MoO3 nanoparticles: solution combustion synthesis, photocatalytic and electrochemical properties. RSC Adv 4:56784–56780
33. Shakir I, Shahid M, Yang HW, Kang DJ (2010) Structural and electrochemical characterization of α-MoO3 nanorod-based electrochemical energy storage devices. Electrochim Acta 56:376–380
34. Mahmooda Q, Yun HJ, Kim WS, Park HS (2013) Highly uniform deposition of MoO_3 nanodots on multiwalled carbon nanotubes for improved performance of supercapacitors. J Power Sources 235: 187–192
35. Hanlon D, Backes C, Higgins T, Hughes JM, O'Neill A, King PJ, McEvoy N, Duesberg GS, Sanchez BM, Pettersson H, Nicolosi V, Coleman JN (2014) Production of molybdenum trioxide nanosheets by liquid exfoliation and their application in high-performance supercapacitors. Chem Mater 26:1751–1763
36. Tao T, Chen QY, Hu HP, Chen Y (2012) MoO_3 nanoparticles distributed uniformly in a carbon matrix for supercapacitor applications. Mater Lett 66:102–105
37. Thangasamy P, Ilayaraja N, Jeyakumar D, Sathish M (2017) Electrochemical cycling and beyond: unrevealed activation of MoO_3 for electrochemical hydrogen evolution reactions. Chem Commun 53:2245–2248
38. Mahmood Q, Yun HJ, Kim WS, Park HS (2013) Highly uniform deposition of MoO_3 nanorods on multiwalled carbon nanotubes for improved performance of supercapacitors. J Power Sources 235: 187–192

39. Chen Z, Cummins D, Reinecke BN, Clark E, Sunkara MK, Jaramillo TF (2011) Core-shell MoO_3-MoS_2 nanowires for hydrogen evolution: a functional design for electrocatalytic materials. Nano Lett 11:4168–4175
40. Sangeetha DN, Selvakumar M (2018) Active-defective activated carbon/MoS_2 composites for supercapacitor and hydrogen evolution reactions. Appl Surf Sci 453:132–140
41. Yan X, Jia Y, Odedairo T, Zhao X, Jin Z, Zhub Z, Yao X (2016) Activated carbon becomes active for oxygen reduction and hydrogen evolution reactions. Chem Commun 52:8156–8159
42. Sun L, Wang L, Tian C, Tan T, Xie Y, Shi K, Li M, Fu H (2012) Nitrogen-doped graphene with high nitrogen level via a one-step hydrothermal reaction of graphene oxide with urea for superior capacitive energy storage. RSC Adv 2:4498–4506
43. Phuruangrat A, Hamb DJ, Thongtem S, Lee JS (2009) Electrochemical hydrogen evolution over MoO_3 nanowires produced by the microwave-assisted hydrothermal reaction. Electrochem Commun 11:1740–1743
44. Pan W, Tian R, Jin H, Guo Y, Zhang L, Wu X, Zhang L, Han Z, Liu Z, Li J, Rao G, Wang H, Chu W (2010) Structure, optical, and catalytic properties of novel hexagonal metastable h-MoO_3 nano- and microrods synthesised with modified liquid-phase processes. Chem Mater 22:6202–6208
45. Chithambararaj A, Bose AC (2011) Investigation on structural, thermal, optical and sensing properties of meta-stable hexagonal MoO_3 nanocrystals of the one-dimensional structure. Beilstein J Nanotechnol 2:585–592
46. Ramana CV, Atuchin VV, Troitskaia IB, Gromilov SA, Kostrovsky VG, Saupe GB (2009) Low-temperature synthesis of morphology-controlled metastable hexagonal molybdenum trioxide (MoO_3). Solid State Commun 149:6–9
47. Chithambararaj A, Yogamalar NR, Bose AC (2016) Hydrothermally synthesized h-MoO_3 and α-MoO_3 nanocrystals: new findings on crystal-structure-dependent charge transport. Cryst Growth Des 16:1984–1995
48. Mai L-Q, Yang F, Zhao Y-L, Xu X, Xu L, Luo Y-Z (2011) Hierarchical $MnMoO_4$/$CoMoO_4$ heterostructured nanowires with enhanced supercapacitor performance. Nat Commun 2:381
49. Sudhakar YN, Hemant H, Nitinkumar SS, Poornesh P, Selvakumar M (2016) Green synthesis and electrochemical characterization of rGO-CuO nanocomposites for supercapacitor applications. Ionics 23:1267–1276
50. Peng H, Ma G, Mu J, Sunb K, Lei Z (2014) Low-cost and high energy density asymmetric supercapacitors based on polyaniline nanotubes and MoO_3 nanobelts. J Mater Chem A 2:10384–10388
51. Zhang X, Zeng X, Yang M, Qi Y (2014) Investigation of a branchlike MoO_3/polypyrrole hybrid with enhanced electrochemical performance used as an electrode in supercapacitors. ACS Appl Mater Interfaces 6:1125–1130
52. Ji H, Liu X, Liu Z, Yan B, Chen L, Xie Y, Liu C, Hou W, Yang G (2015) In situ preparation of sandwich MoO_3/C hybrid nanostructures for high-rate and ultralong-life supercapacitors. Adv Funct Mater 25:1886–1894
53. Chang J, Jin M, Yao F, Kim TH, Le VT, Yue H, Gunes F, Li B, Ghosh A, Xie S, Lee YH (2013) Asymmetric supercapacitors based on graphene/MnO_2 nanospheres and graphene/MoO_3 nanosheets with high energy density. Adv Funct Mater 23:5074–5083
54. Pujari RB, Lokhande VC, Kumbhar VS, Chodankar NR, Lokhande CD (2016) Hexagonal microrods architecture MoO_3 thin film for supercapacitor application. J Mater Sci Mater Electron 27:3312–3317
55. Jiang J, Liu J, Peng S, Qian D, Luo D, Wang Q, Tiana Z, Liu Y (2013) Facile synthesis of α-MoO_3 nanobelts and their pseudocapacitive behavior in an aqueous Li_2SO_4 solution. J Mater Chem A 1:2588–2594
56. Taberna PL, Simon P, Fauvarque JF (2003) Electrochemical characteristics and impedance spectroscopy studies of carbon – carbon supercapacitors. J Electrochem Soc 15:A292–A300
57. Sudhakar YN, Selvakumar M, Bhat DK (2013) $LiClO_4$-doped plasticized chitosan and poly (ethylene glycol) blend as biodegradable polymer electrolyte for supercapacitors. Ionics 19:277–285
58. Conway BE, Tilak BV (2002) Interfacial processes involving electrocatalytic evolution and oxidation of H_2, and the role of chemisorbed H. Electrochim Acta 47:3571–3594
59. Lennon D, Lundie DT, Jackson SD, Kelly GJ, Parker SF (2002) Characterization of activated carbon using X-ray photoelectron spectroscopy and inelastic neutron scattering spectroscopy. Langmuir 18:4667–4673